

Extraction of multimodal dispersion curves from ambient noise with compressed sensing

Lina Gao^{1,2}, Wenqiang Zhang², Zhenguo Zhang² and Xiaofei Chen²

¹Harbin Institute of Technology, Harbin, China

²Department of Earth and Space Sciences, Southern University of Science and Technology, Shenzhen, China

Key Points:

- We present a novel method to extract multimodal dispersion curves from ambient noise with compressed sensing.
- We validate our method by implementing both synthetic tests and field examples.
- Our method of extracting multimodes is very efficient and has a high resolution.

Corresponding author: Xiaofei Chen, chenxf@sustech.edu.cn

Abstract

Although higher-mode surface wave dispersion curves can provide additional constraints on the subsurface velocity structure, their extraction from ambient noise data remains more intractable than the extraction of fundamental-mode dispersion curves. Recently, the frequency-Bessel transform (F-J) method was developed to extract multimodal dispersion curves from ambient noise. Here, we propose an alternative compressed sensing (CS) method for extracting multimodes from ambient noise. We solve the CS inverse problem by using two methods: an l_1 -based optimization algorithm and a Bayesian method. Synthetic and field data examples are conducted to validate our method. The dispersion curves extracted by our method are consistent with those extracted by the F-J method, but our method is more efficient and can extract higher-resolution dispersion energy images than the F-J method. Our method can quickly and reliably extract multimodes from ambient noise, thereby facilitating studies of ambient noise tomography.

1 Introduction

In the mid-1900s, Aki (Aki, 1957, 1965) presented the spatial autocorrelation (SPAC) method for the extraction of dispersion curves from microtremors. More recently, studies have shown that the Green's function between two stations can be obtained from the cross-correlation function (CCF) between the ambient noise recorded by the two stations (Shapiro & Campillo, 2004; Sabra et al., 2005a, 2005b; Roux et al., 2005). Owing to this discovery, ambient noise tomography has been extensively used to measure the Earth's structure in both engineering and seismic tomography (Shapiro et al., 2005; Y. Yang et al., 2007; Gou  dard et al., 2008; Yao et al., 2008; Nunziata et al., 2009). Compared with traditional surface wave tomography, ambient noise tomography has a superior resolution for imaging the shallow crustal structure due to the retrieval of shorter-period measurements and the availability of more interstation paths (Shapiro & Campillo, 2004; Shapiro et al., 2005; Yao et al., 2006). However, previous works mostly used the fundamental mode to tomographically image the subsurface, and thus, the inversion suffered from nonuniqueness and low accuracy. This problem can be alleviated by the inclusion of overtones; that is, the addition of higher modes to the inversion can improve the resolution of the inversion model, strengthen the inversion stability, and obtain information about the deeper subsurface (Xia et al., 2000; Wu et al., 2020). Moreover, for shallow seismic surface waves, due to large contrasts in material properties, higher modes dominate in some frequency

ranges or the dispersion curves exhibit osculation points (Forbriger, 2003b). Consequently, higher modes may easily be mistaken for the fundamental mode; in this case, a subsequent inversion would lead to an unrealistic subsurface model (Forbriger, 2003a). Therefore, it is important to develop a high-resolution method to extract multimodes from seismic data.

However, the extraction of multimodal dispersion curves from seismic data in the multimodal inversion of surface waves has always constituted a challenge. Over the past few decades, many methods using array data, such as the SPAC method (Aki, 1957, 1965), the phase-shift method (Park et al., 1998), the $\tau-p$ transform (McMechan & Yedlin, 1981), the frequency-wavenumber (F-K) transform (Capon, 1969; Lacoss et al., 1969), the high-resolution linear Radon transform (Luo et al., 2008) and the frequency-Bessel transform (F-J) method (Wang et al., 2019), have been developed to extract multimodes. All these methods except the SPAC technique and F-J transform use an exponential base function to transform the wavefield, implying the assumption of plane wave propagation (Wang et al., 2019). In contrast, the SPAC and F-J methods use the Bessel function as the base function and can represent 3-D wave propagation in real-world problems (Wang et al., 2019). However, while the F-J method can effectively extract multimodal dispersion curves from ambient noise and seismic waveform data (Wang et al., 2019; Z. Yang et al., 2019; Li & Chen, 2020), the F-J method is time-consuming since the frequency-Bessel spectrogram is calculated by a discrete summation of the interstation distances for each given frequency. In addition, the resolution of the spectrogram obtained by the F-J method is not sufficient, especially in the low-frequency domain. These shortcomings motivate us to find a new high-resolution method to effectively extract multimodal dispersion curves from ambient noise data.

Compressed sensing (CS) provides a novel sampling paradigm to recover sparse signals and thus has been widely used in diverse fields, such as signal processing and imaging problems (Candes et al., 2006; D. Donoho, 2006; Candes & Wakin, 2008). The key idea of CS is that sparse signals can be exactly recovered from far fewer measurements than required by the classic Shannon theorem (Candes et al., 2006; D. Donoho, 2006; Candes & Wakin, 2008). The extraction of dispersion curves, which represents a sparse signal recovery problem, is solvable within the CS framework. Consequently, CS has been used to effectively extract the dispersion curves of acoustic waves in underwater environments (Dremeau et al., 2017; Le Courtois & Bonnel, 2015), of Rayleigh waves in en-

gineering applications (Z. Chen et al., 2018), and of ultrasonic guided waves in structural health monitoring (Harley & Moura, 2013; Harley, 2016).

In this work we present a new method to extract the multimodal dispersion curves of Rayleigh waves from ambient noise based on CS theory. In our method, the Bessel function as the base function represents 3-D wave propagation in a horizontal layered medium, which is in accordance with the practical situation. Multimodal dispersion curves are recovered from only a small number of CCFs by two CS methods: an l_1 -based algorithm and a Bayesian method. We then compare these two CS methods with the F-J method in terms of the noise level, efficiency and resolution by leveraging synthetic and real-world examples.

2 Method

Considering an elastic layered half-space, the Green's function corresponding to an isotropic source can be expressed as (Luco & Apsel, 1983; Hisada, 1994; X. Chen, 1999; Wang et al., 2019)

$$G_{zz}(r, \omega) = \int_0^{+\infty} g_z(k, \omega) J_0(kr) k dk \quad (1)$$

where $g_z(k, \omega)$ is a kernel function, $J_0(kr)$ is the zeroth-order Bessel function of the first kind, r is the distance between two stations, ω is the angular frequency, and k is the wavenumber. In addition, we know that the relationship between the CCF of ambient noise recorded at two stations and the Green's function between these two stations can be represented as (Sanchez-Sesma & Campillo, 2006; Snieder et al., 2007),

$$C_{zz}(r, \omega) = a \cdot \text{Im}\{G_{zz}(r, \omega)\} \quad (2)$$

where a is a constant and $C_{zz}(r, \omega)$ is the Fourier transform of the CCF of ambient noise between the two stations separated by an interstation distance r . Substituting $k = \frac{\omega}{c}$ (c is the phase velocity) into equation (1) and combining the result with equation (2), we have

$$C_{zz}(r, \omega) = a \int_0^{+\infty} g_{zi}\left(\frac{\omega}{c}, \omega\right) J_0\left(\frac{\omega r}{c}\right) \frac{\omega^2}{c^3} dc \quad (3)$$

where $g_{zi}\left(\frac{\omega}{c}, \omega\right)$ represents the imaginary part of the kernel function. Replacing the integration in equation (3) by a discrete summation, we obtain

$$C_{zz}(r, \omega) = a \sum_{j=1}^n g_{zi}\left(\frac{\omega}{c_j}, \omega\right) J_0\left(\frac{\omega r}{c_j}\right) \frac{\omega^2}{c_j^3} \Delta c_j \quad (4)$$

where Δc_j is the sampling interval and n is the number of discretized points in the phase velocity domain. Here, we adopt a constant sampling interval $\Delta c = (c_n - c_1)/(n - 1)$. The selection of the minimum phase velocity c_1 and the maximum phase velocity c_n depends on the scale of the study area and should contain all the modes of dispersion curves of Rayleigh waves. Note that since dispersion points are singular points of the kernel function (Wang et al., 2019), only at the actual phase velocities with which Rayleigh waves propagate does the kernel function $g_{zi}(\frac{\omega_0}{c}, \omega_0)$ tend toward a limited large value, while at other phase velocities, the values of the kernel function are very small and nearly zero for a certain frequency ω_0 . In other words, the kernel function $g_{zi}(\frac{\omega_0}{c}, \omega_0)$ is sparse in the phase velocity domain: $g_{zi}(\frac{\omega_0}{c}, \omega_0)$ has only s nonzero entries, and $s \ll n$. This property of $g_{zi}(\frac{\omega_0}{c}, \omega_0)$ satisfies the first prerequisite of CS theory, i.e., sparsity (Candes et al., 2006; D. Donoho, 2006). The second prerequisite of CS theory is the restricted isometry property (RIP), and this condition can be met by a randomly selected measurement matrix (Candes & Tao, 2005; Candes & Wakin, 2008; R. Baraniuk et al., 2008). Therefore, considering the CCFs for m randomly selected station pairs among all the station pairs in the study area, we have

$$\begin{bmatrix} C_{zz}(r_1, \omega) \\ C_{zz}(r_2, \omega) \\ \vdots \\ C_{zz}(r_m, \omega) \end{bmatrix} = a\omega^2\Delta c \begin{bmatrix} J_0(\frac{\omega r_1}{c_1})\frac{1}{c_1^3} & J_0(\frac{\omega r_1}{c_2})\frac{1}{c_2^3} & \cdots & J_0(\frac{\omega r_1}{c_n})\frac{1}{c_n^3} \\ J_0(\frac{\omega r_2}{c_1})\frac{1}{c_1^3} & J_0(\frac{\omega r_2}{c_2})\frac{1}{c_2^3} & \cdots & J_0(\frac{\omega r_2}{c_n})\frac{1}{c_n^3} \\ \vdots & \vdots & \ddots & \vdots \\ J_0(\frac{\omega r_m}{c_1})\frac{1}{c_1^3} & J_0(\frac{\omega r_m}{c_2})\frac{1}{c_2^3} & \cdots & J_0(\frac{\omega r_m}{c_n})\frac{1}{c_n^3} \end{bmatrix} \begin{bmatrix} g_{zi}(\frac{\omega}{c_1}, \omega) \\ g_{zi}(\frac{\omega}{c_2}, \omega) \\ \vdots \\ g_{zi}(\frac{\omega}{c_n}, \omega) \end{bmatrix} \quad (5)$$

Writing equation (5) in matrix form and noting that a is unknown in the real world, we obtain

$$\mathbf{C}_{zz} = \mathbf{A}\mathbf{I}_z \quad (6)$$

where the ij th element of \mathbf{A} is $\omega^2\Delta c J_0(\frac{\omega r_i}{c_j})\frac{1}{c_j^3}$ and \mathbf{I}_z is the so-called F-J spectrogram of Wang et al. (2019) with the j th element equal to $a g_{zi}(\frac{\omega}{c_j}, \omega)$. The number of selected CCFs is less than the number of candidate phase velocities, that is, $m < n$. The recovery of the sparse F-J spectrogram \mathbf{I}_z is an underdetermined inverse problem and can be solved using the following formula:

$$\hat{\mathbf{I}}_z = \arg \min_{\mathbf{I}_z} (\|\mathbf{C}_{zz} - \mathbf{A}\mathbf{I}_z\|_2 + \lambda \|\mathbf{I}_z\|_0) \quad (7)$$

where λ is the damping parameter that makes a tradeoff between the data fitting term and the sparsity constraint. However, solving (7) is nonconvex and NP-hard (Candes & Tao, 2005; R. G. Baraniuk, 2007). Many other methods are used to solve the CS inverse

problem and are divided into three main classes: 1) greedy algorithms that find an element or a set of elements of the measurement matrix that best match the residual between the original signal and the current approximation to the signal in each iteration until a stopping condition is met (Tropp & Gilbert, 2007; D. L. Donoho et al., 2012), 2) algorithms that replace the l_0 norm in the sparsity constraint with the l_1 norm to obtain a convex optimization problem that can be solved by many standard procedures (S. S. Chen et al., 1998; D. Donoho et al., 2006), and 3) Bayesian algorithms that consider the recovery of a sparse signal as a Bayesian inference problem assuming a sparsity-inducing prior (Wipf & Rao, 2004; Ji et al., 2008; Z. Zhang & Rao, 2011). In this work, we use the latter two methods to solve the CS reconstruction problem. One method is the l_1 -based optimization algorithm. That is, the recovery problem of equation (7) becomes

$$\hat{\mathbf{I}}_z = \arg \min_{\mathbf{I}_z} (\|\mathbf{C}_{zz} - \mathbf{A}\mathbf{I}_z\|_2 + \lambda \|\mathbf{I}_z\|_1) \quad (8)$$

This can be efficiently solved by linear programming algorithms; we utilize CVX, a MATLAB-based package for convex optimization (Grant & Boyd, 2014). The other method is the Bayesian CS (BCS) algorithm of Ji et al. (2008), who used a fast relevance vector machine (RVM) algorithm for the Bayesian CS inversion. In our work, the F-J spectrogram \mathbf{I}_z is recovered by the l_1 or BCS methods for each given frequency, and the results at each frequency are assembled into the whole F-J spectrogram. The amplitude peaks of the F-J spectrogram correspond to the locations of the sought Rayleigh wave dispersion curves.

3 Tests with synthetic data

We first design two synthetic tests to validate the above proposed CS methods for extracting multimodal dispersion curves from ambient seismic noise. Similar to the F-J method, our method is independent of the scale of the study region, and thus, we choose two small-scale models for the synthetic tests. First, we synthesize ambient noise data for a given 1-D velocity model. Then, we use the F-J method, l_1 -based method and BCS method to construct the dispersion curves from the synthetic ambient noise and compare the results of these three methods.

3.1 Model with a low-velocity layer

The first synthetic test model (Model 1) is the same as that utilized by previous studies (Ikeda et al., 2012; Wang et al., 2019; Hu et al., 2020) and is composed of four

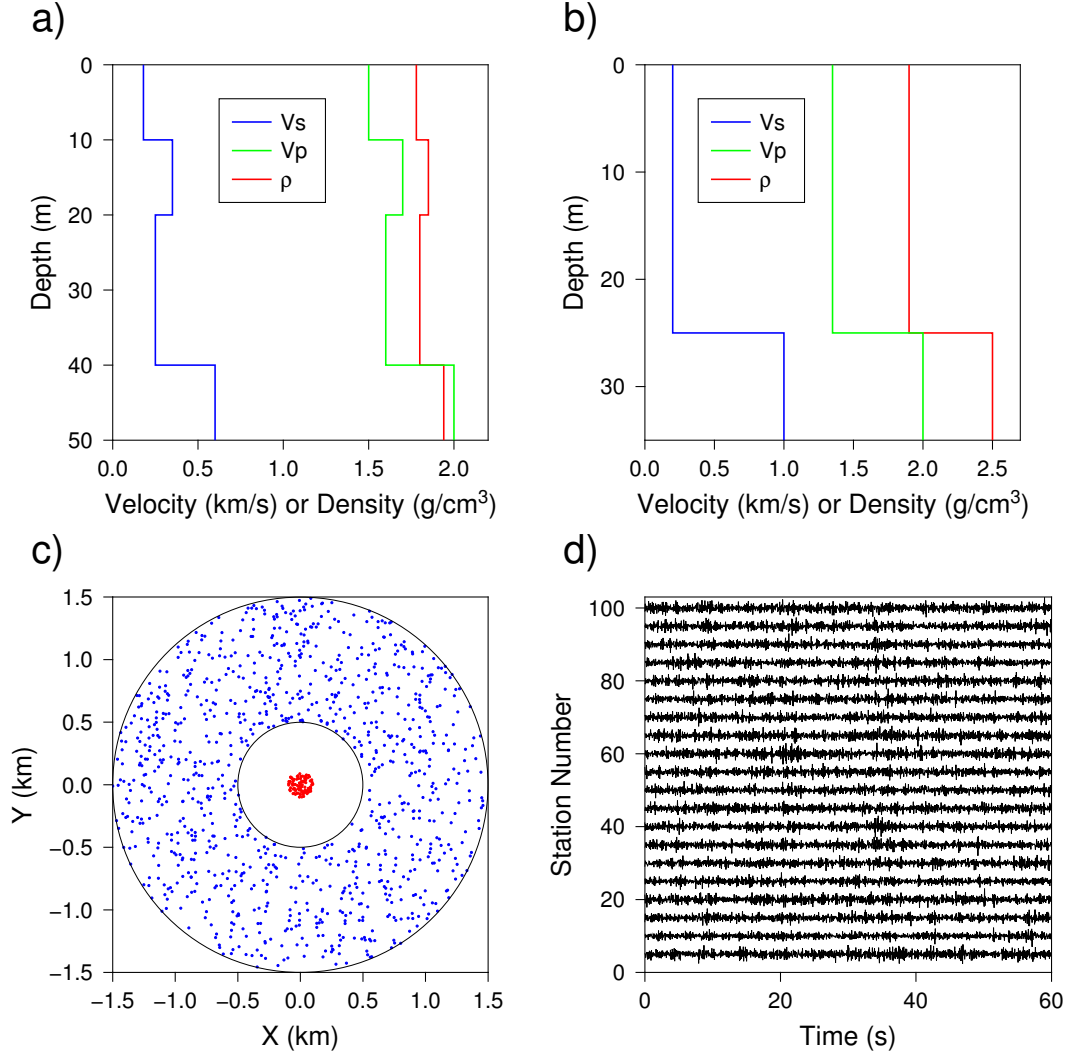


Figure 1. (a) Model 1 and (b) Model 2 used in the synthetic tests. (c) Distributions of the sources (blue dots) and stations (red dots). (d) Synthetic ambient noise records of some stations.

layers with a low-velocity layer (Figure 1a, Table 1). We first follow the same procedure as that of Wang et al. (2019) to synthesize the ambient noise. The distributions of the stations and sources are shown in Figure 1c. As shown in Figure 1c, 100 stations are randomly located in a circle with a radius of 0.1 km, and all 1000 sources are on the free surface and randomly distributed within a ring with an inner radius of 0.5 km and an outer radius of 1.5 km. We use a vertical point single force source with the Ricker wavelet as the source time function. The center frequency of each source is randomly chosen in the range of 6-10 Hz, the source amplitude is randomly set in the range of 0-1, and the source shift time is randomly distributed in the range of 0-65 s. The generalized reflection-transmission coefficient method (GRTM) (X. Chen, 1993, 1999; H.-M. Zhang et al., 2003) is used to compute the theoretical seismograms for a given 1-D velocity model. Then, we synthesize ambient seismic noise data by stacking the theoretical seismograms excited by all the sources for each station. Finally, we obtain 60 s-long vertical component records of ambient noise with an effective frequency range of 2.5-25 Hz. The synthetic ambient noise records of some stations are shown in Figure 1d.

We then separately apply the F-J method, l_1 -based method and BCS method to image the dispersion curves from the synthetic ambient noise of Model 1. For the F-J method, we use the CCFs of all the station pairs to calculate the F-J spectrogram. For the l_1 -based method, we randomly select the CCFs of 500 station pairs from among the CCFs of all station pairs to extract the dispersion curves. Note that for the l_1 -based method, the value of the tradeoff parameter λ is important for finding a reasonable solution to equation (8). We select a proper λ value by using the L-curve criterion for each frequency in the range of 2.5-25 Hz. We select $\lambda = 1e - 6$ for $f < 5$ Hz and $\lambda = 5e - 6$ for $f \geq 5$ Hz based on the computation of L-curves at different frequencies. The L-curves for two frequencies are shown as examples in Figure 2. For the BCS method, we use the same CCF measurements employed in the l_1 -based method to compare the results of the two CS methods. The F-J spectrograms obtained by the three methods are shown in Figure 3. The image of the Rayleigh wave dispersion energy obtained by the F-J method (Figure 3a) is generally consistent with the results of Wang et al. (2019) and Hu et al. (2020). In the image obtained by the F-J method (Figure 3a), we can identify the Rayleigh wave fundamental mode in the frequency range of 2.5-25 Hz, the first overtone in the frequency ranges of 4.5-7.5 and 19.5-25 Hz, the second overtone in the small frequency range of 18.3-19.5 Hz, and an osculation between the first and second overtones at 19.5 Hz. The

Table 1. Parameters of the two models in the synthetic tests

	Thick (m)	ρ (kg/m ³)	Vs (m/s)	Vp (m/s)	Q
Model 1	10	1,780	180	1,500	10000
	10	1,850	350	1,700	10000
	20	1,800	250	1,600	10000
	∞	1,940	600	2,000	10000
Model 2	25	1,900	200	1,350	10000
	∞	2,500	1,000	2,000	10000

frequency ranges of the dispersion curves obtained by the l_1 -based and BCS methods are almost the same as those obtained by the F-J method, and the dispersion curves extracted by the three methods all agree well with the theoretical dispersion curves computed by the GRTM (Figure 3).

It is worth noting that the resolution of the dispersion energy images obtained by the l_1 -based and BCS methods is much higher than that obtained by the F-J method, especially for the low-frequency part (Figure 3). This result may benefit from the pursuit of a sparse solution in the l_1 -based and BCS methods. Another interesting thing is that the images of the dispersion curves obtained by the l_1 -based and BCS methods contain less noise than that obtained by the F-J method, and the spectrogram of the BCS method is the cleanest among the results of the three methods. Notably, sidelobes parallel to the fundamental mode and having smaller amplitudes than the fundamental mode in the F-J image are not observed in the CS images (Figure 3), which may be due to the use of the sparse constraint in the latter. Finally, to compare the computation times of the three methods, we run the three methods on the same personal computer without using sophisticated parallel acceleration technology. For each method, we calculate the F-J spectrogram for the same numbers of phase velocities and frequencies. The computation times of the three methods are shown in Table 2. The most time-consuming algorithm is the F-J method, followed by the l_1 -based method, while the BCS method takes the least time, which reflects the high efficiency of the CS methods.

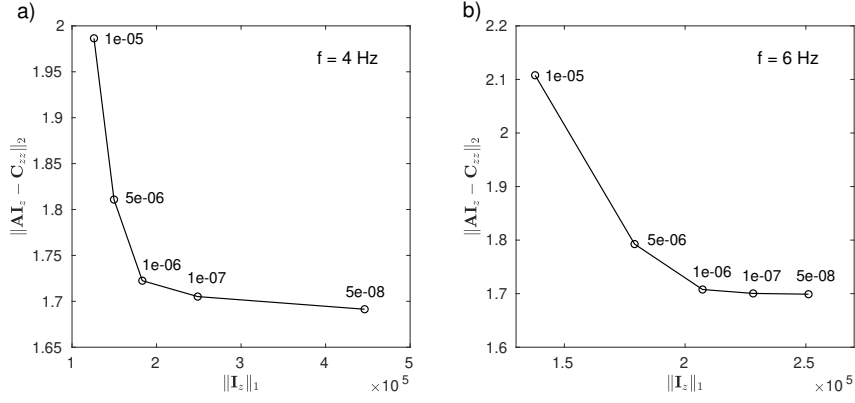


Figure 2. L-curves between the residual misfit and the model $l1$ norm at (a) $f = 4$ Hz and (b) $f = 6$ Hz.

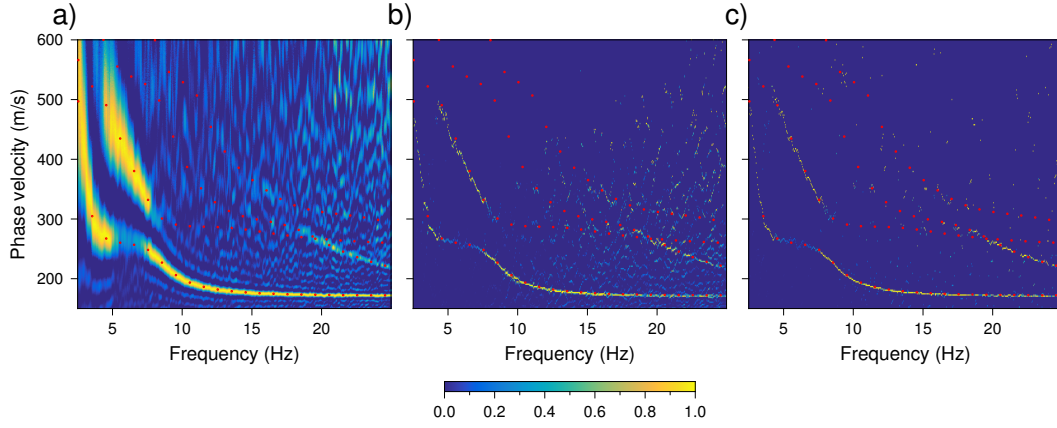


Figure 3. Reconstruction of the dispersion curves for Model 1 by (a) the F-J method; (b) the $l1$ -based method; and (c) the BCS method. Red dots are the theoretical dispersion curves.

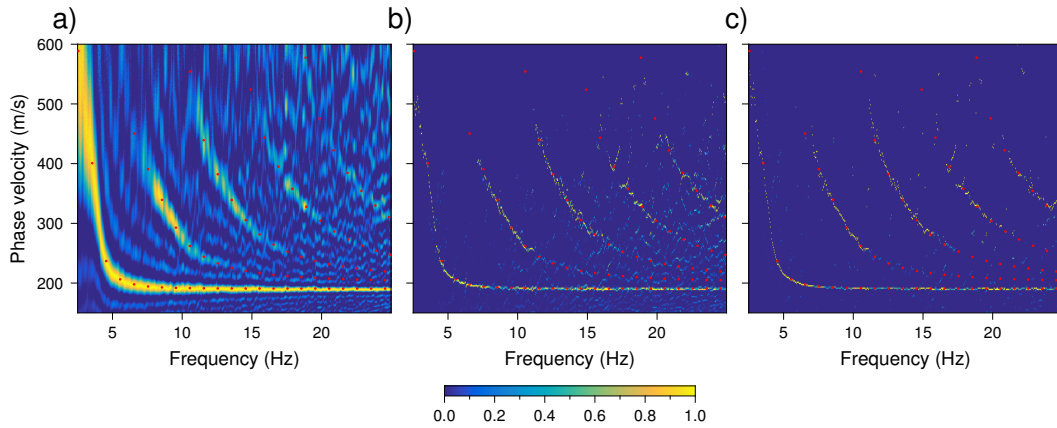
3.2 Model with two layers

The second synthetic test model (Model 2) contains two layers representing soil overlying a half-space (Figure 1b, Table 1). The model is the same as that in Hu et al. (2020). Again, we use the above method to synthesize the ambient noise of Model 2. Similarly, we then apply the three methods to the synthetic ambient noise. The dispersion curve images reconstructed by the three methods are shown in Figure 4. The main features of the image extracted by the F-J method are similar to the results of Hu et al. (2020), but there are some differences in the frequency range where the overtones can be iden-

Table 2. Computation time for each example

	F-J	l_1	BCS
Model 1	1229.6 s	413.9 s	44.2 s
Model 2	1233.6 s	404.4 s	44.1 s
Eastern NCC	2443.2 s	781.3 s	351.2 s
Eastern US	1614.2 s	715.9 s	281.8 s

167 tified (Figure 4a). This may be caused by the different approaches for synthesizing the
 168 ambient noise, including the different methods employed to calculate the synthetic seis-
 169 mograms and the different source distributions. Up to five dispersion curves can be clearly
 170 identified in the image extracted by the F-J method (Figure 4a). The dispersion curves
 171 in the images obtained by the l_1 -based and BCS methods are similar to those obtained
 172 by the F-J method, and the dispersion curves obtained by the three methods are all con-
 173 sistent with the theoretical dispersion curves (Figure 4). Again, the spectrograms ob-
 174 tained by the CS methods have a higher resolution than that obtained by the F-J method
 175 (Figure 4). The BCS method produces the dispersion image with the least noise and takes
 176 the shortest computation time, followed by the l_1 -based method, while the F-J method
 177 obtains the noisiest image and takes the longest computation time (Figure 4, Table 2).
 178 These results are obtained because these CS methods use a sparsity constraint, fewer sta-
 179 tion pairs and highly efficient inversion algorithms.

**Figure 4.** Same as Figure 3 but for Model 2.

4 Application to real data

To further verify the effectiveness and practicability of the CS methods, we apply our method to two real datasets. One field dataset was recorded by stations located in the eastern North China Craton (NCC), and the other dataset was recorded by USArray stations in the eastern United States. We first calculate the CCFs from the ambient noise data in these two areas and then extract the dispersion curves from the CCFs of the two areas using the F-J, l_1 -based and BCS methods and finally compare the results of the three methods.

4.1 Field data from the eastern NCC

For the first field data example, we use the continuous vertical component records from 102 stations in the eastern NCC (Figure 5a) for the entire year of 2007. First, before computing the CCFs, we preprocess the raw ambient noise data following the process presented in Bensen et al. (2007). Because the stations are of the same type, we do not remove the instrument response. We downsample the daily ambient noise records to 5 Hz and remove the mean and trend of each daily segment. Then, the ambient noise is bandpass filtered between the periods of 0.6 s and 200 s. To reduce the effects of non-stationary sources, especially earthquake signals, and to broaden the band of CCFs, we apply temporal normalization and spectral whitening to the ambient noise data. Second, we compute the daily CCFs between all available station pairs and stack all the CCFs for the same station pair. The stacked CCFs of some station pairs are shown in Figure 5b; the Rayleigh wave signals can be clearly identified in the CCFs. The CCFs are almost temporally symmetric, and we use the positive lag parts of the CCFs to extract the dispersion curves. We sort the spectral CCFs by their interstation distances in ascending order for further computation.

Finally, we apply the F-J, l_1 -based and BCS methods to extract the dispersion curves from the spectral CCFs. For the F-J method, we use the CCFs of all station pairs. For the l_1 -based method, we randomly select 1000 CCFs from among the CCFs of all station pairs. More CCFs are used in the eastern NCC than in the above synthetic tests because the CCFs retrieved from the real data have a lower signal-to-noise ratio than the synthetic data. For the BCS method, we use the same 1000 randomly selected CCFs to compare the results of the CS methods. The images recovered by the three methods

are illustrated in Figure 5d-f. The results of the three methods are roughly similar. The low-frequency part of the fundamental mode (0.02-0.25 Hz) is clear, whereas the high-frequency part (0.25-0.5 Hz) is blurred. In addition to the fundamental mode, six overtones can be recognized in the images. It is worth noting that there are obvious differences among these results (Figure 5d-f). Compared with the image obtained by the F-J method, the dispersion images obtained by the CS methods have a higher resolution (the distribution of dispersion energy is narrower), which is very important for reducing the error when picking phase velocities. These findings also show that the CS methods can suppress noise better than the F-J method. Moreover, unlike the F-J image, there are no obvious sidelobes parallel to the dispersion curves or aliasing interfering with the dispersion curves in the CS images (Figure 5d-f). Furthermore, the dispersion energy in the image obtained by the BCS method is more continuous and concentrated than that obtained by the $l1$ -based method (Figure 5e-f). This shows that the BCS method is more stable when dealing with noisy real-world data.

Next, we average the 3-D S-wave velocity (V_s) model of Shen et al. (2016) in the study area to obtain a local 1-D V_s model (Figure 5c). The P-wave velocity (V_p) and density models are calculated using the empirical formulas of Brocher (2005). The theoretical dispersion curves computed from the 1-D discretized velocity model basically agree with the dispersion curves extracted by the three methods (Figure 5d-f). However, there are mismatches between the theoretical dispersion curves and extracted dispersion curves for some modes, such as the fundamental mode in the frequency range of 0.2-0.5 Hz and two higher modes, namely, the fifth higher mode and the sixth higher mode. This shows that the average 1-D V_s model of Shen et al. (2016) may not accurately describe the true underground velocity structure. Hence, it is necessary to add higher modes to the inversion of surface waves to provide more constraints on the velocity structures.

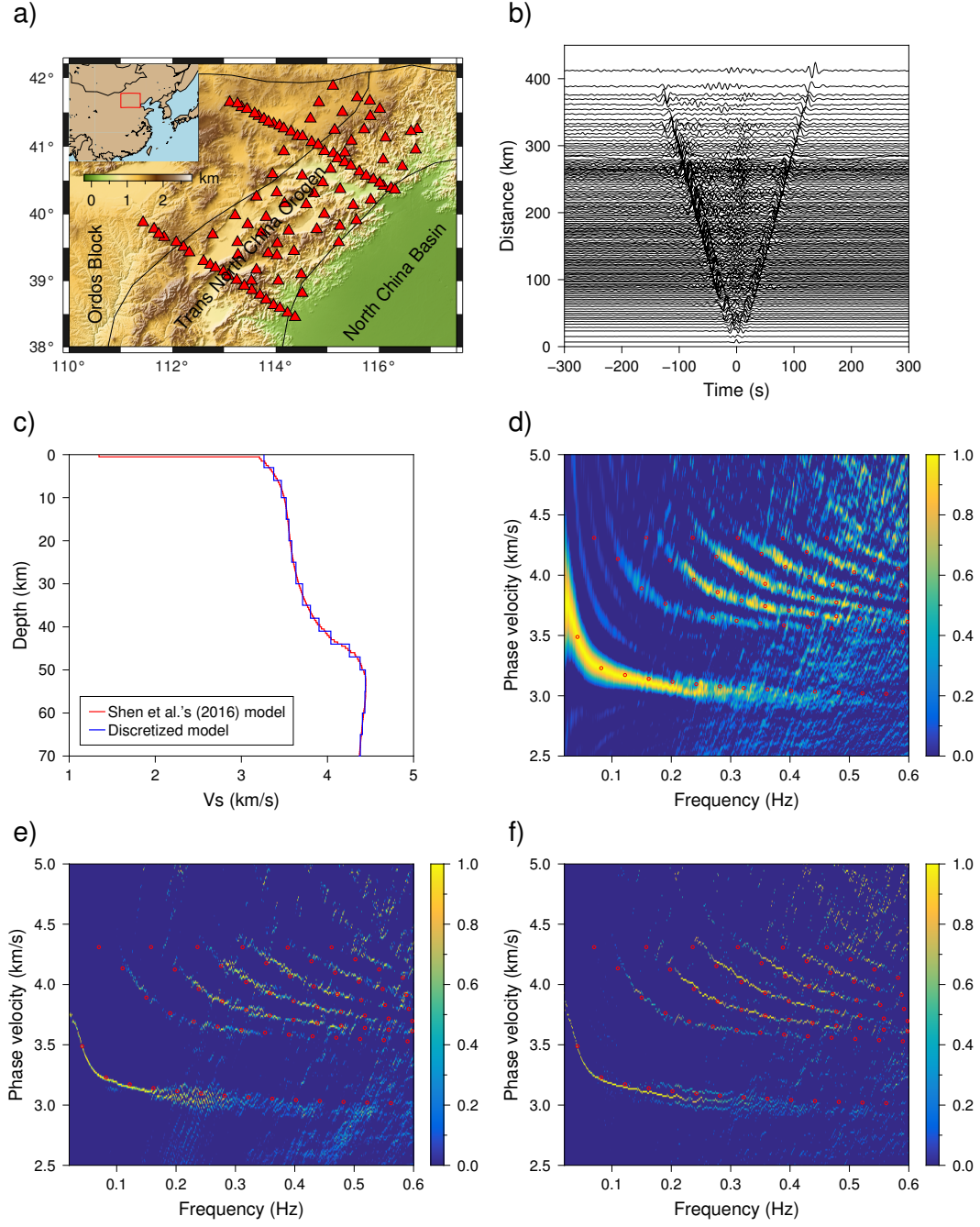


Figure 5. (a) Distribution of stations in the eastern NCC. Red triangles represent stations; the red rectangle in the inset map shows the location of the study area. (b) Ambient noise CCFs of some station pairs in the period band of 2-50 s. (c) The 1-D Vs model (red line) obtained by averaging the 3-D Vs model of Shen et al. (2016) in the study area and its discretized model (blue line). The F-J spectrograms extracted by (d) the F-J method; (e) the l_1 -based method; and (f) the BCS method. In (d)-(f), the red dots are the theoretical dispersion curves calculated from the discretized average model of Shen et al. (2016).

4.2 Field data from the eastern United States

For the second field data application, we use the vertical components recorded by 93 USArray Transportable Array stations in the eastern United States (Figure 6a) from 1 June 2011 to 1 December 2011. We use the same stations as those employed in the first application of Wu et al. (2020). We cut the continuous records to a length of one day and remove the instrument response of each daily segment. The following data processing procedure is the same as that in the first example of field data described above. We compute and stack the daily CCFs between all possible station pairs, and Rayleigh waves clearly appear in the stacked CCFs (Figure 6b). We again apply the three methods to the positive lag parts of the CCFs, and the images produced by the three methods are shown in Figure 6d-f. The image reconstructed by the F-J method is similar to that presented by Wu et al. (2020). The fundamental mode can be clearly identified in the frequency range of 0.02-0.3 Hz and is split into two branches at 0.3 Hz in the image obtained by the F-J method (Figure 6d). This bifurcation of the fundamental mode may be caused by lateral heterogeneity of the subsurface velocity structure. In addition, six higher modes can be reasonably identified in the low-frequency part (0.2-0.5 Hz) but only vaguely observed in the high-frequency part (0.5-0.6 Hz) (Figure 6d).

Comparing the results of the CS methods with those of the F-J method, we can draw a similar conclusion to that from the first example. The dispersion curves extracted by the CS methods agree well with those extracted by the F-J method (Figure 6d-f). However, the images obtained by the CS methods have a higher resolution than that obtained by the F-J method. In addition, the image from the BCS method contains the least noise, followed by the image from the l_1 -based method, while the image from the F-J method is the noisiest (Figure 6d-f).

The 1-D Vs model (Figure 6c) is obtained by averaging the 3-D Vs model of Shen and Ritzwoller (2016) in the study area. The Vp and density models are calculated by the empirical formulas of Brocher (2005). The dispersion images obtained by the three methods coincide well with the theoretical dispersion curves computed from the average discretized 1-D velocity model except for some higher modes in the low-frequency range (the fourth and fifth higher modes in 0.29-0.32 Hz and 0.34-0.37 Hz, respectively) (Figure 6d-f). This result again shows the importance of extracting higher-mode dispersion curves and including them in the inversion.

For the two applications of field data, the computation times of the three methods are shown in Table 2. As in the two synthetic examples, the BCS method takes the shortest computation time owing to using the CCFs of fewer station pairs and adopting the fast and efficient RVM algorithm, followed by the l_1 -based method, which similarly uses the CCFs of relatively few station pairs, and finally, the F-J method takes the longest computation time because it employs the CCFs of all station pairs. These field data examples take more computation time than the synthetic tests (Table 2) because the CCFs of more station pairs are utilized to suppress the noise of the dispersion images when dealing with real data.

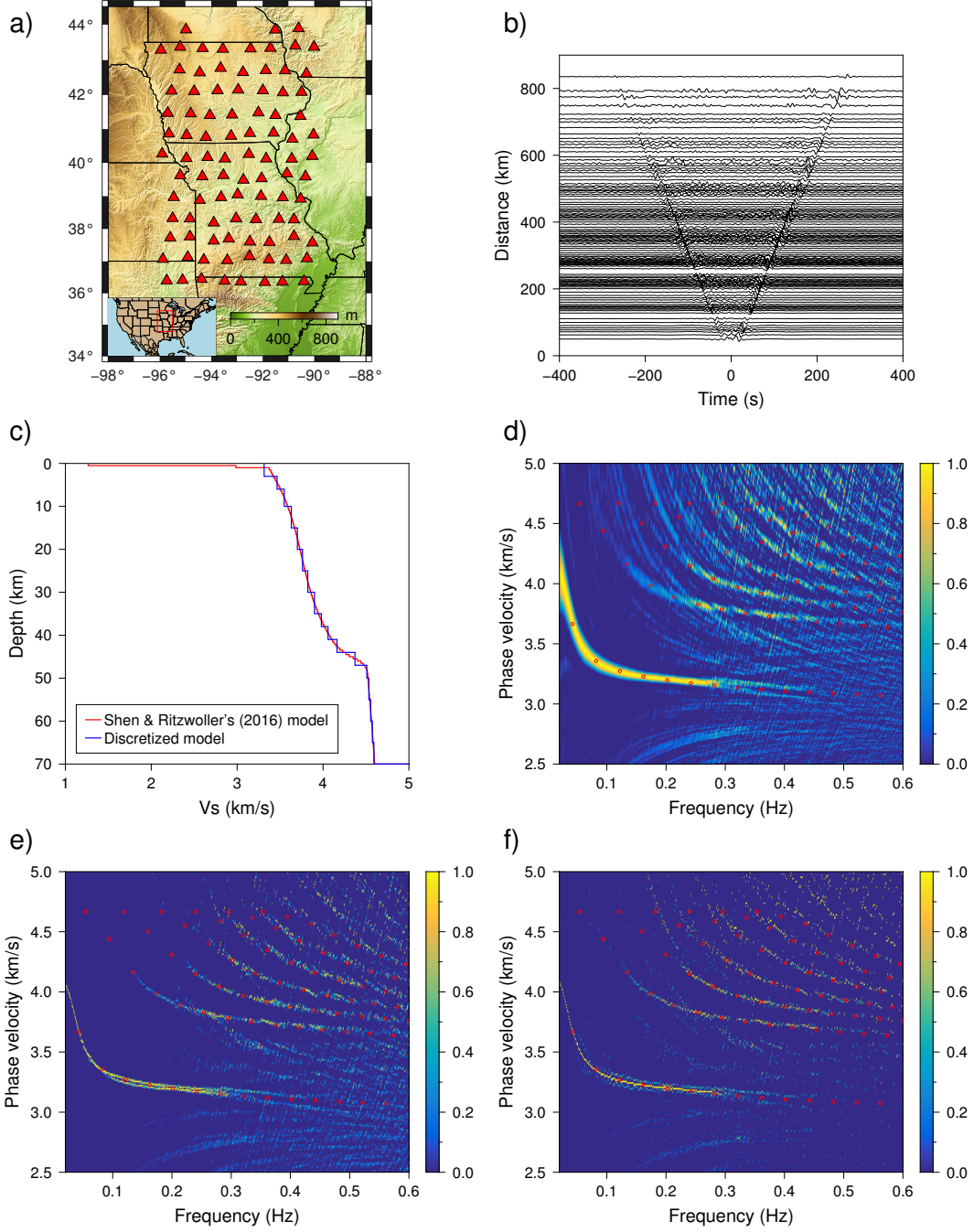


Figure 6. Similar to Figure 5 but for the eastern United States. In (c), the red line is the 1-D average Vs model of Shen and Ritzwoller (2016), and the blue line is the corresponding discretized model.

5 Discussion and conclusions

We present CS methods to extract Rayleigh wave multimodal dispersion curves from ambient noise. We validate the new methods on both synthetic data and real datasets

from the eastern NCC and the eastern United States. The tests on the synthetic and field data demonstrate that (1) the dispersion curve images obtained by the CS methods have a higher resolution than that obtained by the F-J method; (2) the image from the BCS method has the lowest noise level, followed by the l_1 -based method and finally by the F-J method; and (3) the BCS method has the highest computational efficiency, followed by the l_1 -based and F-J methods. As a result, the proposed CS methods can quickly and accurately extract multimodal dispersion curves, which is crucial for the inversion of multimodal dispersion curves to obtain a more reliable velocity structure.

For the F-J method, the F-J spectrogram is calculated by integrating over interstation distances which is approximated by a discrete summation. According to the Nyquist-Shannon theorem, the interstation distance coverage should be dense to avoid aliasing for the F-J method. However, only a small number of random measurements are needed to recover a sparse signal in CS theory. Since small numbers of CCFs are used, the computation time is reduced for the CS methods. Furthermore, for the CS images, the true dispersion curves with relatively large amplitudes are resolved, while noise with small amplitudes in the F-J image, such as aliasing and sidelobes, is not present in the CS images; this may be due to the sparse constraint used in the CS methods. In addition, the resolution of the spectrogram increases with the implementation of the sparse constraint in the CS methods.

In this work, we apply two CS methods to the CCFs computed from ambient noise. We use fewer CCFs that are randomly selected from among all available CCFs for the extraction of multimodal dispersion curves. In future work, CS methods can be used to image multimodal dispersion curves from seismograms in engineering applications or earthquake event data. CS methods can reduce the number of stations used and can quickly obtain high-resolution dispersion curve images.

Acknowledgments

The waveform data was provided by China Seismic Array Data Management Center at Institute of Geophysics, China Earthquake Administration (<http://www.chinarraydmc.cn/>) and by the IRIS Data Management Center (<http://ds.iris.edu/ds/nodes/dmc/data/types/waveform-data/>). The reference models of Shen et al. (2016) and Shen and Ritzwoller (2016) are downloaded from <http://ciei.colorado.edu/Models/> and <http://>

ds.iris.edu/ds/products/emc-earthmodels/, respectively. This work is supported by the National Natural Science Foundation of China (grants 41922024 and 41790465).

References

- Aki, K. (1957). Space and Time Spectra of Stationary Stochastic Waves, with Special Reference to Microtremors. *Bulletin of the Earthquake Research Institute, University of Tokyo*, 35(3), 415–456.
- Aki, K. (1965, August). A note on the use of microseisms in determining the shallow structure of the Earth’s crust. *Geophysics*, 30(4), 665–666. doi: 10.1190/1.1439640
- Baraniuk, R., Davenport, M., DeVore, R., & Wakin, M. (2008, December). A Simple Proof of the Restricted Isometry Property for Random Matrices. *Constructive Approximation*, 28(3), 253–263. doi: 10.1007/s00365-007-9003-x
- Baraniuk, R. G. (2007). Compressive Sensing [lecture notes]. *IEEE Signal Processing Magazine*, 24(4), 118–121. doi: 10.1109/MSP.2007.4286571
- Bensen, G. D., Ritzwoller, M. H., Barmin, M. P., Levshin, A. L., Lin, F., Moschetti, M. P., ... Yang, Y. (2007). Processing seismic ambient noise data to obtain reliable broad-band surface wave dispersion measurements. *Geophysical Journal International*, 169(3), 1239–1260. doi: 10.1111/j.1365-246X.2007.03374.x
- Brocher, T. M. (2005, December). Empirical Relations between Elastic Wavespeeds and Density in the Earth’s Crust. *Bulletin of the Seismological Society of America*, 95(6), 2081–2092. doi: 10.1785/0120050077
- Candes, E., Romberg, J., & Tao, T. (2006, February). Robust uncertainty principles: Exact signal reconstruction from highly incomplete frequency information. *IEEE Transactions on Information Theory*, 52(2), 489–509. doi: 10.1109/TIT.2005.862083
- Candes, E., & Tao, T. (2005, December). Decoding by Linear Programming. *IEEE Transactions on Information Theory*, 51(12), 4203–4215. doi: 10.1109/TIT.2005.858979
- Candes, E., & Wakin, M. (2008, March). An Introduction To Compressive Sampling. *IEEE Signal Processing Magazine*, 25(2), 21–30. doi: 10.1109/MSP.2007.914731
- Capon, J. (1969). High-resolution frequency-wavenumber spectrum analysis. *Pro-*

- ceedings of the *IEEE*, 57(8), 1408–1418. doi: 10.1109/PROC.1969.7278
- Chen, S. S., Donoho, D. L., & Saunders, M. A. (1998). Atomic decomposition by basis pursuit. *SIAM Journal on Scientific Computing*, 20(1), 33–61. doi: 10.1137/S1064827596304010
- Chen, X. (1993, November). A systematic and efficient method of computing normal modes for multilayered half-space. *Geophysical Journal International*, 115(2), 391–409. doi: 10.1111/j.1365-246X.1993.tb01194.x
- Chen, X. (1999). Seismogram synthesis in multi-layered half-space Part I. Theoretical formulations. *Earthquake Research in China*, 13(2), 149–174.
- Chen, Z., Jiang, B., Song, J., & Wang, W. (2018, July). Accurate Sparse Recovery of Rayleigh Wave Characteristics Using Fast Analysis of Wave Speed (FAWS) Algorithm for Soft Soil Layers. *Applied Sciences*, 8(7), 1204. doi: 10.3390/app8071204
- Donoho, D. (2006, April). Compressed sensing. *IEEE Transactions on Information Theory*, 52(4), 1289–1306. doi: 10.1109/TIT.2006.871582
- Donoho, D., Elad, M., & Temlyakov, V. (2006, January). Stable recovery of sparse overcomplete representations in the presence of noise. *IEEE Transactions on Information Theory*, 52(1), 6–18. doi: 10.1109/TIT.2005.860430
- Donoho, D. L., Tsaig, Y., Drori, I., & Starck, J.-L. (2012, February). Sparse Solution of Underdetermined Systems of Linear Equations by Stagewise Orthogonal Matching Pursuit. *IEEE Transactions on Information Theory*, 58(2), 1094–1121. doi: 10.1109/TIT.2011.2173241
- Dremeau, A., Le Courtois, F., & Bonnel, J. (2017, October). Reconstruction of Dispersion Curves in the Frequency-Wavenumber Domain Using Compressed Sensing on a Random Array. *IEEE Journal of Oceanic Engineering*, 42(4), 914–922. doi: 10.1109/JOE.2016.2644780
- Forbriger, T. (2003a, June). Inversion of shallow-seismic wavefields: II. Inferring subsurface properties from wavefield transforms. *Geophysical Journal International*, 153(3), 735–752. doi: 10.1046/j.1365-246X.2003.01985.x
- Forbriger, T. (2003b, June). Inversion of shallow-seismic wavefields: I. Wavefield transformation. *Geophysical Journal International*, 153(3), 719–734. doi: 10.1046/j.1365-246X.2003.01929.x
- Gouédard, P., Roux, P., & Campillo, M. (2008, March). Small-scale seismic inversion

- 376 using surface waves extracted from noise cross correlation. *The Journal of the*
 377 *Acoustical Society of America*, 123(3), EL26-EL31. doi: 10.1121/1.2838251
- 378 Grant, M., & Boyd, S. (2014, March). *CVX: Matlab software for disciplined convex*
 379 *programming, version 2.1*. <http://cvxr.com/cvx>.
- 380 Harley, J. B. (2016, August). Predictive Guided Wave Models Through Sparse
 381 Modal Representations. *Proceedings of the IEEE*, 104(8), 1604–1619. doi: 10
 382 .1109/JPROC.2015.2481438
- 383 Harley, J. B., & Moura, J. M. F. (2013, May). Sparse recovery of the multimodal
 384 and dispersive characteristics of Lamb waves. *The Journal of the Acoustical*
 385 *Society of America*, 133(5), 2732–2745. doi: 10.1121/1.4799805
- 386 Hisada, Y. (1994). An Efficient Method for Computing Green’s Functions for a Lay-
 387 ered Half-Space with Sources and Receivers at Close Depths. *Bulletin of the*
 388 *Seismological Society of America*, 84(5), 1456–1472.
- 389 Hu, S., Luo, S., & Yao, H. (2020, August). The Frequency-Bessel Spectrograms of
 390 Multicomponent Cross-Correlation Functions From Seismic Ambient Noise.
 391 *Journal of Geophysical Research: Solid Earth*, 125(8), e2020JB019630. doi:
 392 10.1029/2020JB019630
- 393 Ikeda, T., Matsuoka, T., Tsuji, T., & Hayashi, K. (2012, July). Multimode in-
 394 version with amplitude response of surface waves in the spatial autocorre-
 395 lation method. *Geophysical Journal International*, 190(1), 541–552. doi:
 396 10.1111/j.1365-246X.2012.05496.x
- 397 Ji, S., Xue, Y., & Carin, L. (2008, June). Bayesian Compressive Sensing. *IEEE*
 398 *Transactions on Signal Processing*, 56(6), 2346–2356. doi: 10.1109/TSP.2007
 399 .914345
- 400 Lacoss, R. T., Kelly, E. J., & Toksöz, M. N. (1969, February). Estimation of seis-
 401 mic noise structure using arrays. *Geophysics*, 34(1), 21–38. doi: 10.1190/1
 402 .1439995
- 403 Le Courtois, F., & Bonnel, J. (2015, August). Compressed sensing for wideband
 404 wavenumber tracking in dispersive shallow water. *The Journal of the Acousti-*
 405 *cal Society of America*, 138(2), 575–583. doi: 10.1121/1.4926381
- 406 Li, Z., & Chen, X. (2020, March). An Effective Method to Extract Overtones
 407 of Surface Wave From Array Seismic Records of Earthquake Events. *Jour-*
 408 *nal of Geophysical Research: Solid Earth*, 125(3), e2019JB018511. doi:

- 10.1029/2019JB018511
- Luco, J. E., & Apsel, R. J. (1983). On the Green's functions for a layered half-space. Part I. *Bulletin of the Seismological Society of America*, 73(4), 909–929.
- Luo, Y., Xia, J., Miller, R. D., Xu, Y., Liu, J., & Liu, Q. (2008, May). Rayleigh-Wave Dispersive Energy Imaging Using a High-Resolution Linear Radon Transform. *Pure and Applied Geophysics*, 165(5), 903–922. doi: 10.1007/s00024-008-0338-4
- McMechan, G. A., & Yedlin, M. J. (1981). Analysis of dispersive waves by wave field transformation. *Geophysics*, 46(6), 869–874. doi: 10.1190/1.1441225
- Nunziata, C., De Nisco, G., & Panza, G. (2009, May). S-waves profiles from noise cross correlation at small scale. *Engineering Geology*, 105(3-4), 161–170. doi: 10.1016/j.enggeo.2009.01.005
- Park, C. B., Miller, R. D., & Xia, J. (1998, January). Imaging dispersion curves of surface waves on multi-channel record. In *SEG Technical Program Expanded Abstracts 1998* (pp. 1377–1380). Society of Exploration Geophysicists. doi: 10.1190/1.1820161
- Roux, P., Sabra, K. G., Kuperman, W. A., & Roux, A. (2005, January). Ambient noise cross correlation in free space: Theoretical approach. *The Journal of the Acoustical Society of America*, 117(1), 79–84. doi: 10.1121/1.1830673
- Sabra, K. G., Gerstoft, P., Roux, P., & Kuperman, W. A. (2005a). Extracting time-domain Green's function estimates from ambient seismic noise. *Geophysical Research Letters*, 32(3), L03310. doi: 10.1029/2004GL021862
- Sabra, K. G., Roux, P., & Kuperman, W. A. (2005b, January). Arrival-time structure of the time-averaged ambient noise cross-correlation function in an oceanic waveguide. *The Journal of the Acoustical Society of America*, 117(1), 164–174. doi: 10.1121/1.1835507
- Sanchez-Sesma, F. J., & Campillo, M. (2006, June). Retrieval of the Green's Function from Cross Correlation: The Canonical Elastic Problem. *Bulletin of the Seismological Society of America*, 96(3), 1182–1191. doi: 10.1785/0120050181
- Shapiro, N. M., & Campillo, M. (2004, April). Emergence of broadband Rayleigh waves from correlations of the ambient seismic noise. *Geophysical Research Letters*, 31, L07614. doi: 10.1029/2004GL019491
- Shapiro, N. M., Campillo, M., Stehly, L., & Ritzwoller, M. H. (2005, March). High-

- Resolution Surface-Wave Tomography from Ambient Seismic Noise. *Science*, 307(5715), 1615–1618. doi: 10.1126/science.1108339
- Shen, W., & Ritzwoller, M. H. (2016, June). Crustal and uppermost mantle structure beneath the United States. *Journal of Geophysical Research: Solid Earth*, 121(6), 4306–4342. doi: 10.1002/2016JB012887
- Shen, W., Ritzwoller, M. H., Kang, D., Kim, Y., Lin, F.-C., Ning, J., . . . Zhou, L. (2016, August). A seismic reference model for the crust and uppermost mantle beneath China from surface wave dispersion. *Geophysical Journal International*, 206(2), 954–979. doi: 10.1093/gji/ggw175
- Snieder, R., Wapenaar, K., & Wegler, U. (2007, March). Unified Green’s function retrieval by cross-correlation; connection with energy principles. *Physical Review E*, 75(3), 036103. doi: 10.1103/PhysRevE.75.036103
- Tropp, J. A., & Gilbert, A. C. (2007, December). Signal Recovery From Random Measurements Via Orthogonal Matching Pursuit. *IEEE Transactions on Information Theory*, 53(12), 4655–4666. doi: 10.1109/TIT.2007.909108
- Wang, J., Wu, G., & Chen, X. (2019, April). Frequency-Bessel Transform Method for Effective Imaging of Higher-Mode Rayleigh Dispersion Curves From Ambient Seismic Noise Data. *Journal of Geophysical Research: Solid Earth*, 124(4), 3708–3723. doi: 10.1029/2018JB016595
- Wipf, D., & Rao, B. (2004, August). Sparse Bayesian Learning for Basis Selection. *IEEE Transactions on Signal Processing*, 52(8), 2153–2164. doi: 10.1109/TSP.2004.831016
- Wu, G.-x., Pan, L., Wang, J.-n., & Chen, X. (2020, January). Shear Velocity Inversion Using Multimodal Dispersion Curves From Ambient Seismic Noise Data of USArray Transportable Array. *Journal of Geophysical Research: Solid Earth*, 125(1), e2019JB018213. doi: 10.1029/2019JB018213
- Xia, J., Miller, R. D., & Park, C. B. (2000, January). Advantages of calculating shear-wave velocity from surface waves with higher modes. In *SEG Technical Program Expanded Abstracts 2000* (pp. 1295–1298). Society of Exploration Geophysicists. doi: 10.1190/1.1815633
- Yang, Y., Ritzwoller, M. H., Levshin, A. L., & Shapiro, N. M. (2007, January). Ambient noise Rayleigh wave tomography across Europe. *Geophysical Journal International*, 168(1), 259–274. doi: 10.1111/j.1365-246X.2006.03203.x

- 475 Yang, Z., Chen, X., Pan, L., Wang, J., Xu, J., & Zhang, D. (2019). Multi-channel
 476 analysis of Rayleigh waves based on the Vector Wavenumber Transformation
 477 Method (VWTM). *Chinese Journal of Geophysics(in Chinese)*, 62(1), 298–
 478 305. doi: 10.6038/cjg2019M0641
- 479 Yao, H., Beghein, C., & van der Hilst, R. D. (2008, April). Surface wave array
 480 tomography in SE Tibet from ambient seismic noise and two-station analysis
 481 - II. Crustal and upper-mantle structure. *Geophysical Journal International*,
 482 173(1), 205–219. doi: 10.1111/j.1365-246X.2007.03696.x
- 483 Yao, H., van der Hilst, R. D., & de Hoop, M. V. (2006, August). Surface-wave array
 484 tomography in SE Tibet from ambient seismic noise and two-station analysis
 485 - I. Phase velocity maps. *Geophysical Journal International*, 166(2), 732–744.
 486 doi: 10.1111/j.1365-246X.2006.03028.x
- 487 Zhang, H.-M., Chen, X.-F., & Chang, S. (2003). An Efficient Numerical Method
 488 for Computing Synthetic Seismograms for a Layered Half-space with Sources
 489 and Receivers at Close or Same Depths. *Pure and Applied Geophysics*, 160,
 490 467–486. doi: 10.1007/PL00012546
- 491 Zhang, Z., & Rao, B. D. (2011, September). Sparse Signal Recovery With Tempo-
 492 rally Correlated Source Vectors Using Sparse Bayesian Learning. *IEEE Jour-
 493 nal of Selected Topics in Signal Processing*, 5(5), 912–926. doi: 10.1109/JSTSP
 494 .2011.2159773